Inorganic Chemistry

pubs.acs.org/IC Article

Hydroxyl Defects in $LiFePO_4$ Cathode Material: DFT+U and an Experimental Study

Dmitry A. Aksyonov,* Irina Varlamova, Ivan A. Trussov, Aleksandra A. Savina, Anatoliy Senyshyn, Keith J. Stevenson, Artem M. Abakumov, Andriy Zhugayevych, and Stanislav S. Fedotov

Cite This: Inorg. Chem. 2021, 60, 5497−5506

Read Online

ABSTRACT: Lithium iron phosphate, $LiFePO_4$, a widely used cathode material in commercial Li-ion batteries, unveils a complex defect structure, which is still being deciphered. Using a combined computational and experimental approach comprising density functional theory (DFT)+U and molecular dynamics calculations and X-ray and neutron diffraction, we provide a comprehensive characterization of various OH point defects in $LiFePO_4$, including their formation, dynamics, and localization in the interstitial space and at Li, Fe, and P sites. It is demonstrated that one, two, and four (five) OH groups can effectively stabilize Li, Fe, and P vacancies, respectively. The presence of D (H) at both Li and P sites for hydrothermally synthesized deuterium-enriched $LiFePO_4$ is confirmed by joint X-ray and neutron powder diffraction structure refinement at 5 K that also reveals a strong deficiency of P of 6%. The P occupancy decrease is explained by the formation of hydrogarnet-like P/4H and P/5H defects, which have the lowest formation energies among all considered OH defects. Molecular dynamics simulation shows a rich structural diversity of these defects, with OH groups pointing both inside and outside vacant P tetrahedra creating numerous energetically close conformers, which hinders their explicit localization with diffraction-based methods solely. The discovered conformers include structural water molecules, which are only by 0.04 eV/atom H higher in energy than separate OH defects.

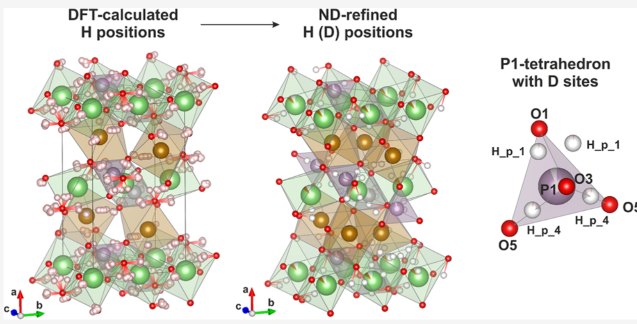

1. INTRODUCTION

The transition to a sustainable world established on renewable energy and electric transport critically depends on the development of efficient and affordable energy storage devices, such as rechargeable batteries. Among existing battery technologies, Li-ion has many advantages in terms of specific energy, longevity, and power, explaining its fast penetration into the fields of portable electronics, electric cars, and grid storage.

One of the commercialized Li-ion technologies relies on $LiFePO_4$ (LFP) cathode material[1] that provides high stability, safety, and affordability. Being well optimized for practical applications, LFP remains a highly important system for studying the impact of phase transformations, defects, and interfaces on electrochemical performance.[2−11] In particular, the influence of Li_{Fe}^{-} and Fe_{Li}^{+} antisite defects on the kinetics of phase transformations and electrochemical behavior of the material is still not fully clear.[12−14]

Contrary to the Li and Fe sites in the cationic sublattice,[15,16] the P site is rarely considered defect-active. It is taken for granted that the PO_4 group is highly stable and that no defects are possible at the P site. Nevertheless, the deficiency of P (up to 8% of P vacancies) was first observed by Amisse et al. in a highly defective LFP, synthesized with a low-temperature co-precipitation method.[17] This seems surprising as the extraction of P results in four undercoordinated oxygens, which should be stabilized by some charge compensation mechanism.

To address this question, the P-deficient LFP was also obtained by Sumanov et al. using hydrothermal synthesis.[18] According to powder X-ray diffraction (PXRD) and neutron diffraction, the obtained samples can contain up to 16% of P vacancies with the refined composition of $Li_{0.93}Fe_{1.07}P_{0.84}O_4$. To maintain the charge balance, this composition should contain 68% of Fe^{3+}. However, Mössbauer spectroscopy showed that the fraction of Fe^{3+} does not exceed 4%. Therefore, it was proposed that the charge balance is maintained by residual water in the form of OH groups inside the P vacancies. Indeed, infrared spectroscopy showed absorption bands characteristic of the structural OH bonds, while thermogravimetric/mass spectrometry analysis confirmed the water loss of the LFP sample in two stages with onsets at 350 and 450 °C, which are much higher compared to the typical temperatures of the adsorbed water loss.

Received: November 3, 2020
Published: April 8, 2021

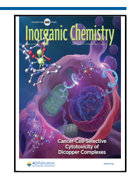

https://doi.org/10.1021/acs.inorgchem.0c03241
Inorg. Chem. 2021, 60, 5497−5506

Additionally, the density functional theory (DFT) calculations showed that the formation of PO_4/O_4H_n (n = 1−4) defects is feasible under the synthesis conditions.[18]

The existence of OH defects in LFP can be envisaged by drawing parallels with its structural analogues in the olivine mineral group (Mg,Fe)SiO_4, where the Si site is equivalent to the P site in LFP. It is well known that almost any olivine mineral sample contains structural water, which is also stored in the form of point defects, including OH-stabilized Si vacancies.[19] From the very beginning, it was proposed that the OH groups and Si vacancies form hydrogarnet-like (Si/4H) defects,[20,21] which were later confirmed by DFT calculations to be the lowest-energy defects in the forsterite (Mg_2SiO_4) representative of the olivine group.[22] However, in many studies it was suggested that OH groups can reside in Mg and Fe sites as well.[23,24] A recent thermodynamic DFT study found that the relative stability of Mg/2H and Si/4H defects in forsterite depends on pressure and temperature.[25]

From this perspective, the discovery of P/4H defects in LFP suggests that there exist many commonalities between defective structures of the two crystal groups. In particular, it remains unclear whether OH groups reside in Li and Fe vacancies of LFP. Another important question is related to the dynamics of OH defects and their possible conformers, as up to now the experimental methods had not been able to precisely localize and confirm the OH defects in the structure of either LFP or olivine minerals.

In this study, we provide a detailed investigation of OH defects in LFP using DFT and DFT+U methods, which proved their usefulness to study cathode materials.[26] We extend the pool of considered defects with interstitial H and OH defects in Li and Fe vacancies, as well as 5H defects in P. To study the dynamics of defects and their possible conformers, we apply ab initio molecular dynamics (MD) simulations. The structural refinement of the defective, hydrothermally prepared deuterium- and ^{7}Li-enriched LFP sample was carried out based on joint X-ray and room- and low-temperature (5 K) neutron powder diffraction data.

In Section 2, we provide details of our calculations, thermodynamic model, and experiment; in Section 3 we report on static calculations of defects; and in Section 4, the ab initio MD investigation of defects. In Section 5, we provide experimental confirmation of modeling results and conclude with discussions in Section 6.

2. METHODS

2.1. Computational Details. DFT calculations were performed using the projected augmented plane-wave method, with the Vienna ab initio simulation package[27] and the high-throughput Python-based package SIMAN.[28] We adopted the spin-polarized generalized gradient approximation (GGA) exchange-correlation functional of the Perdew, Burke, and Ernzerhof form.[29] Only ferromagnetic configurations were considered since the influence of antiferromagnetic ordering on geometry and substitution energies of OH defects is negligible ($\lesssim$0.01 eV, Supporting Information Table S9). To account for the localized nature of Fe 3d electrons, the DFT+U method with a rotationally invariant approximation was used.[30] The U value for Fe was set to 4.0 eV.[31] The energy cutoff was 400 eV (PREC = Accurate in the VASP code), the k-point spacing was less than 0.3 Å^{-1}, and the maximum force acting on each atom after relaxation was less than 0.05 eV/Å. For the density of states (DOS) calculation, the spacing of k-points was 0.15 Å^{-1}. Such a computational setup provides the 0.02 eV precision for substitution energies of OH defects; see Table S10.

The interstitial hydrogen defects were considered using one LFP unit cell. The substitution hydrogen defects (Li/H, Fe/2H, and P/4H) were considered using a 1 × 2 × 2 LFP supercell. The optimization of the size and the shape of simulation cells was performed for ideal LFP and a supercell with one P vacancy. For other cases, including all H-defective supercells, only optimization of atomic positions was performed with lattice vectors taken from the ideal LFP, since the influence of cell optimization on OH formation energies was found to be negligible ($\lesssim$0.02 eV).

MD simulations of hydroxyl defects were performed in a 1 × 2 × 2 supercell within NVT ensemble using a Nose thermostat as implemented in VASP. To reach the required simulation timescales, the accuracy of electronic structure calculations was reasonably reduced: the plane-wave cutoff was set to 300 eV, Gaussian smearing with 0.2 eV width was used, and the SCF-convergence criteria were loosened (EDIFF = 10^{-3}, also PREC = Low in VASP code). This accuracy reduction introduces an acceptable error of up to 0.12 eV in the substitution energies of OH defects; see Table S11. The MD time step is 1 fs. For each initial condition, at least 10 MD trajectories were generated. Most of the MD runs were performed at 900 K, corresponding to the typical annealing temperature. MD was started with relaxed geometries, and, in this case, the system typically came to a quasi-equilibrium within 1 ps; see Figure S12. For this reason, statistical analysis was performed for data collected after 1 ps.

The formation energy of a vacancy X is defined as

$$E_{\mathrm{vac}} = E(\mathrm{LFP},\ V_{\mathrm{X}}) - E(\mathrm{LFP}) + \mu(\mathrm{X}) \tag{1}$$

where $E(\mathrm{LFP}, V_X)$ is the total energy of the LFP supercell containing one X vacancy, $E(\mathrm{LFP})$ is the total energy of the supercell with an ideal LFP structure, and $\mu(\mathrm{X})$ is the atomic chemical potential of species X.

The hydrogen solution energy in interstitial voids is defined as

$$E_{\mathrm{sol}} = E(\mathrm{LFP},\ \mathrm{H}) - E(\mathrm{LFP}) - \mu(\mathrm{H}) \tag{2}$$

where $E(\mathrm{LFP}, \mathrm{H})$ is the total energy of the LFP supercell containing interstitial H in one of the available voids. The H substitution energy is defined as

$$E_{\mathrm{sub}} = [E(\mathrm{LFP},\ mV_{\mathrm{X}},\ n\mathrm{H}) - E(\mathrm{LFP}) + m\mu(\mathrm{X}) - n\mu(\mathrm{H})]/n \tag{3}$$

where m is 0 or 1 and n is the number of hydrogen atoms. The chemical potentials $\mu(\mathrm{X})$ as a function of oxygen chemical potential are shown in Figure S2.

The thermodynamic constraints for chemical potentials of species were determined using the equilibrium Li−Fe−P−O_2 phase diagram, constructed by Ong et al. on the basis of DFT+U calculations.[32] The phase diagram was rationalized in terms of oxygen chemical potential $\mu(O_2)$, the value of which determines the end and intermediate members of the full phase diagram. According to the phase diagram, in full agreement with experimental data, LFP is stable in a wide range of oxidation environments. We considered a region of the phase diagram formed by Li_3PO_4, $LiFePO_4$, and Fe2O_3 end members corresponding to Li-excess conditions, relevant for LFP synthesis. This region remains intact for $\mu(O_2)$ ranging from −13.1 to −11.5 eV (Figures 2−4 in ref 32), which was chosen in this study for estimating the stability of vacancies and OH defects. Here, $\mu(O_2)$ is an external variable; therefore, no correction for the O_2 overbinding error caused by DFT was used. The chemical potential of hydrogen was defined from the assumption that hydrotriphylite is in equilibrium with the gas phase of water. The definitions of $\mu(\mathrm{X})$ are provided in Supporting Information Section S2. The formation energies of OH defects are provided for $\mu(O_2) = -13.1$ eV if otherwise not stated.

Though the end members on the adopted phase diagram do not fully correspond to the hydrothermal synthesis conditions, the LFP samples are typically annealed in a reducing atmosphere, where the $\mu(O_2)$ is defined by temperature and O_2 partial pressure. Therefore, the phase diagram is valid for studying the energetics of point defects irrelevant to the synthesis method.

2.2. Synthesis. The P-deficient $LiFePO_4$ was synthesized via a hydrothermal route at a low concentration of initial reagents.[18] The prepared solutions of ^{7}LiOH (0.0075 mol, NCCP, 98%) and H_3PO_4 (0.0025 mol, Reakhim, 98%) in D_2O (Kurchatov Institute, 99.8%) were

https://doi.org/10.1021/acs.inorgchem.0c03241
Inorg. Chem. 2021, 60, 5497−5506

Table 1. Calculated Lattice Parameters (Å), Volume (Å^3), Magnetic Momentum on Fe (μ_B), and the Average Potential (V) for $LiFePO_4$

Source	*a*	*b*	*c*	*V*	μ	Potential
PBE	10.38	6.06	4.75	299	3.61	2.96
PBE+*U* (*U* = 4.0 eV)	10.41	6.07	4.75	301	3.77	3.45
PBE[35]	10.39	6.04	4.75	298	3.54	2.99
PBE+*U* (*U* = 3.71 eV)[35]	10.42	6.07	4.76	301	3.73	3.47
PBE+*U* (*U* = 4.3 eV)[36]	10.46	6.08	4.75	302		
exp[1]	10.33	6.01	4.69	291		3.50

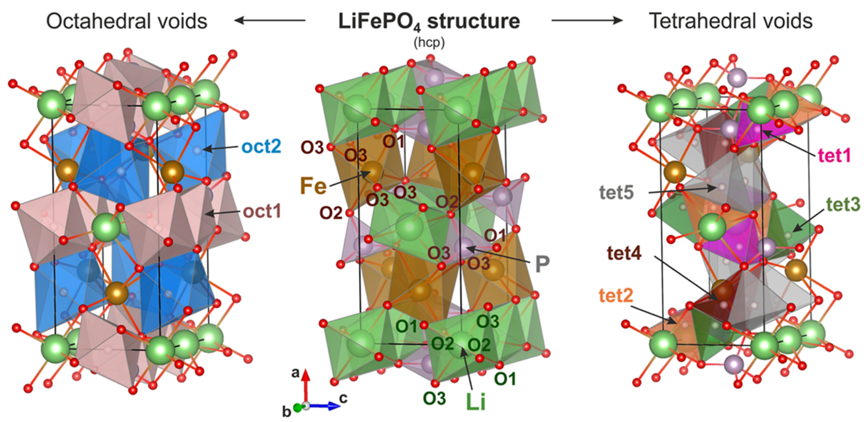

Figure 1. Crystal structure of $LiFePO_4$ showing all available, filled, and empty polyhedral units.

first mixed to form a Li_3PO_4 precipitate. Then, $FeSO_4{\cdot}7H_2O$ (0.0025 mol, Component reaktiv, 98%) and ascorbic acid (0.0025 mol, Reakhim, 98%) were dissolved separately in D_2O, mixed, and added to the Li_3PO_4-contained solution in a 1:1 volume ratio. After stirring for 15 min, the reaction mixture was transferred to a Teflon-lined autoclave with 2/3 of the occupied autoclave volume (100 mL). The autoclave was sealed under an Ar atmosphere, heated to 200 °C, kept at this temperature for 12 h, and cooled down to room temperature. The resulting product was separated via centrifugation, washed with deionized water, and then dried at 40 °C for 12 h under vacuum.

Assuming the same volume distribution of ^{1}H/D in the reaction media, we expect 99.8% D of hydrogen purity in the resulting phase.

2.3. Diffraction Study Details. The structure of the obtained sample was studied using X-ray powder diffraction (Bruker D8 Advance) equipped with a Cu X-ray tube ($\lambda_{K\alpha1}$ = 1.5406 Å, $\lambda_{K\alpha2}$ = 1.5444 Å). Neutron diffraction patterns were collected using a high-resolution powder diffractometer SPODI[33] in Forschungs-Neutronenquelle Heinz Maier-Leibnitz (FRM II) at the Technical University of Munich at a wavelength of 1.5482 Å. The data were collected in the range from 2 to 152° 2Θ at room (298 K) and low (5 K) temperature. Si standard data were used for calibration. The joint Rietveld refinement was performed using Bruker-AXS-TOPAS-V software with routines of TOPAS-Academic.[34] The thermal analysis was performed on a thermogravimetry-differential scanning calorimetry (TG−DSC) F3 STA-449 apparatus (Netzsch, Germany) combined with a mass spectrometer QMS 403 D Aëolos (Netzsch, Germany) under He flow. The sample was heated at a 5 K/min rate in the 30−800 °C temperature range.

3. FORMATION ENERGIES OF POINT DEFECTS IN $LIFEPO_4$

3.1. Lattice Parameters and the Electronic Structure of $LiFePO_4$. The calculated lattice parameters for $LiFePO_4$ are provided in Table 1. They are in agreement with computational and experimental literature data. There is a minor difference between PBE and PBE+*U* results.

The calculated site-projected partial density of states (PDOS) for PBE and PBE+*U* are shown in Supporting Information Figure S3. The PDOS agrees well with the literature.[37−40] The Fe atom is in high-spin $t_{2g}(\downarrow)$ $t_{2g}^3(\uparrow)$ $e_g^2(\uparrow)$ (Fe^{2+}) state. The $t_{2g}(\downarrow)$ electron is strongly localized just below the Fermi level. The band gap for PBE and PBE+*U* are 0.4 and 3.5 eV, respectively. The comparison of the calculated and experimental band gaps is discussed in Supporting Information Section S3, which shows that the exact value of the LFP band gap is still under debate in the literature. However, for this study, it is of secondary importance, since no excited states are considered. At the same time, the computed DOS below the Fermi level, having an explicit influence on bonding, is in good agreement with experimental X-ray photoelectron spectroscopy (XPS) studies.[41]

3.2. Li, Fe, and P Vacancies. As the first step, we calculate formation energies of vacancies for all sites. Even at the most oxidizing chemical potentials, the formation of vacancies is unfavorable. Their energies for Li, Fe, and P amount to 0.40, 1.40, and 3.46 eV, respectively. The value obtained for the Li vacancy is in agreement with Hoang et al., where the energy of V_{Li}^{-} + Fe_{Fe}^{+} for the most oxidizing condition is 0.32 eV.[16] While the Li vacancy has relatively low formation energy, the formation of Fe or P vacancies is much less probable. For example, the equilibrium concentration of the P vacancies at room temperature should be less than 10^{-36}, which is almost undetectable. At more reducing conditions (corresponding to lower $\mu(O_2)$), the formation energies are even larger since they are directly proportional to the $-\mu(O_2)$.

It should be noted that the formation of vacancies is accompanied by the oxidation of neighboring Fe to 3+. There are one, two, and five Fe^{3+} for Li, Fe, and P vacancies, respectively. Fe^{3+} is well localized and usually bound to the undercoordinated oxygen atoms left after vacancy formation. The binding is explained by the fact that undercoordinated oxygen atoms repel from each other and reduce distances to neighboring Fe cations. At the same time, the Fe oxidation is

https://doi.org/10.1021/acs.inorgchem.0c03241
Inorg. Chem. 2021, 60, 5497−5506

characterized by the contraction of Fe−O bonds. Therefore, the oxidation of Fe near the vacancy allows for the minimization of local stresses (see Supporting Information Section S4 for more details).

3.3. One H in Ideal LFP. In addition to Li, Fe, and P positions, the LFP lattice contains several voids per formula unit coordinated by oxygen: two octahedral (oct1, oct2) and seven tetrahedral voids with only five being symmetrically non-equivalent (tet1−tet5). These voids are suitable candidates for H dissolution (see Figure 1 and Supporting Information Section S4). Since the tetrahedral voids are quite small, for guessing the H position we considered only the void center. The subsequent atomic optimization shows that only three configurations are stable with the lowest solution energy of 3.1 eV. In all of these cases, hydrogen bonds to Fe, ending up between tetrahedral and octahedral voids. The solution energies, optimized positions, and Fe−H distances are collected in Table 2. The atomic structure of H_i(pos1) is shown in Figure 2. In this case, hydrogen shows anionic nature forming a slightly polar covalent bond with Fe (see Figure S4). Though the formation of hydrogen-transition metal bonds seems unusual for oxygen-containing compounds, this phenomenon is observed in $LaSrCoO_3H_{0.7}$[42] and $BaTiO_{3-x}H_x$ ($x \leq 0.6$).[43]

Table 2. DFT+U Calculated Solution E_{sol} and Relative E_{rel} Energies (eV) for Interstitial H in $LiFePO_4$ ($\mu(O_2) = -13.1$ eV)[a]

Defect	Initial	Optimized	d_{Fe-H}	E_{sol}	E_{rel}
H_i(pos1)	tet2 or tet3	tet2/oct2(F)	1.55	3.1	0
H_i(pos2)	tet1	tet1/oct2(F)	1.56	3.4	0.3
H_i(pos3)	tet4 or tet5	tet4/oct2(E)	1.53	3.5	0.4
H_i(pos1′)	oct2 at O1	tet2/oct2(F)	1.55	3.1	0
H_i(pos4)	oct2 at O3	tet5/oct2(F)	2.27	4.2	1.1
H_i(pos5)	oct1 at O2	octFe tet5/octLi(F)	1.66	3.5	0.4
H_i(pos6)	oct1 at O1	tet5/tet4(E)	2.70	3.7	0.5

[a]The initial and optimized positions are provided. After optimization, the H atom is located either on the face (F) or the edge (E) shared by two voids. d_{Fe-H} gives the shortest Fe−H distance (Å).

In the case of much larger octahedral voids, a hydrogen atom was placed at a 1 Å distance near each oxygen atom pointing toward one of the opposite oxygens inside the void, with 12 configurations in total. During optimization, the H atom moves away from the initial position, resulting in seven locally stable configurations. The four most relevant configurations are collected in Table 2. The lowest-energy configuration H_i(pos1′) is equivalent to that obtained by starting from the tetrahedral void, H_i(pos1), while H_i(pos4) and H_i(pos6) are unique in the way that H forms a 1 Å bond with O3 and O1, respectively. Interestingly, in the case of H_i(pos6), Li moves to one half of its octahedral void away from hydrogen. Overall, it is seen that the lowest solution energy is 3.1 eV, showing that the H solution in ideal LFP is rather improbable. The coordinates of H atoms are available in Supporting Information structural files.

3.4. One and Two H at Li and Fe Vacancies. To find the most stable position of H at the Li vacancy, we considered three symmetry-unique positions denoted as O1, O2, and O3. The lowest-energy configuration is shown in Figure 2, where the H atom is bonded to the O2 atom pointing to the octahedral void left after Li removal. The H−O1 distance and O2−H−O1 angle are 1.95 Å and 146°, respectively. The H position is displaced toward tet4 and tet5 voids.

The hydrogen solution energy E_{sol} inside the Li vacancy is −0.34 eV, which is much lower compared to that of the interstitial voids, suggesting that partially understoichiometric LFP is more appropriate to absorb hydrogen. However, the E_{sub} is 0.90 eV, showing that the substitution of Li by H in the most reducing Li-excess environment is still endothermic.

The Fe^{2+} in $LiFePO_4$ can be substituted by two H without the change of the oxidation state of other iron atoms. Among nine symmetry-unique configurations of two hydrogens in four oxygen sites O1, O2, O3a, O3b (there are two nonequivalently coordinated O3 sites around Fe vacancy), the lowest one has hydrogens bonded to the O3a oxygens, pointing inside the octahedral void left after Fe removal, toward O3b, as shown in Figure 2. The E_{sub} is 0.89 eV per H atom, which is very close to the substitution energy of Li by H (Table 3).

3.5. Four and Five H at P Vacancy. A phosphorus vacancy with 4 H atoms is different because there are four oxygen sites (O1, O2, and two O3) and four hydrogens, the low-energy configurational space includes various orientations of the OH groups, and there is formation of a H_2O molecule bonded to Fe. By considering different starting configurations, several metastable P/4H cases were obtained, which are collected in Table 3. One of the representative structures (hh1, hydrogarnet) is shown in Figure 2. Three H atoms point inside the tetrahedron left after P removal, and one H bound to O1 points to the largest tetrahedral void tet2 located near the Li-diffusion saddle point. The Fe atom connected with two O3 oxidizes to Fe^{3+}, allowing for contraction of two Fe−O bonds at the same time. This Fe^{3+} can be attributed to the small hole polaron.[44,45] The substitution energy of the hh1 defect is 0.54 eV per H,

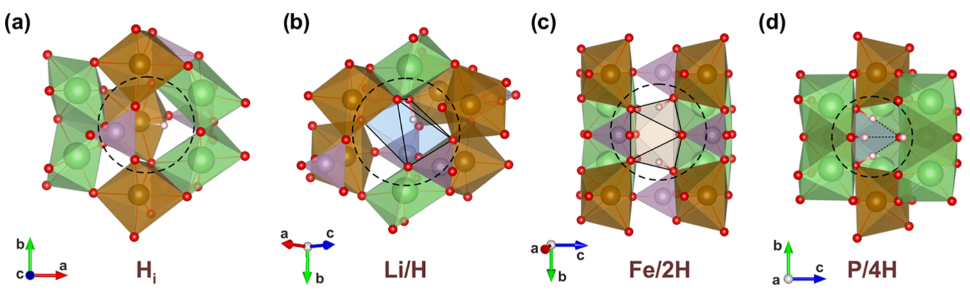

Figure 2. (a) Lowest-energy position of H in ideal $LiFePO_4$. H forms bonds with Fe and is located at the face shared by octahedral void oct2 and tetrahedral void tet2. H atoms are depicted as gray spheres. (b) Lowest-energy position of H in Li vacancy of $LiFePO_4$. H forms bonds with O2 oxygen. (c) Lowest-energy position of two H in the Fe vacancy of $LiFePO_4$. H atoms are bound to O3a. (d) hh1 configuration of four H in the P vacancy of $LiFePO_4$. Three H are located inside the P vacancy and the fourth H is in the tet2 void.

https://doi.org/10.1021/acs.inorgchem.0c03241
Inorg. Chem. 2021, 60, 5497−5506

Table 3. Calculated Substitution Energies (eV) of Defects in $LiFePO_4$ at Two Different $\mu(O_2)$

Defect	$\mu(O_2) = -11.5$ eV		$\mu(O_2) = -13.1$ eV	
	GGA+*U*	GGA	GGA+*U*	GGA
$V_{Li}^{-} + Fe_{Fe}^{+}$	0.41	−1.43	1.01	−0.84
$V_{Fe}^{2-} + 2Fe_{Fe}^{+}$	1.41	−1.96	2.60	−0.77
$V_{P}^{5-} + 5Fe_{Fe}^{+}$	3.45	0.33	4.83	1.72
H_{Li}^{0}	0.70	0.31	0.90	0.51
$(2H)_{Fe}^{0}$	0.69	0.29	0.89	0.49
$(4H)_{P}^{-} + Fe_{Fe}^{+}$ (hh1)	0.59	0.54	0.54	0.49
$(4H)_{P}^{-} + Fe_{Fe}^{+}$ (hh2)	0.56	0.50	0.51	0.45
$(4H)_{P}^{-} + Fe_{Fe}^{+}$ (w1)	0.60	0.50	0.55	0.45
$(4H)_{P}^{-} + Fe_{Fe}^{+}$ (w2)	0.63	0.53	0.58	0.48
$(5H)_{P}^{0}$ ($w1_5$)	0.56	0.80	0.44	0.68

which is notably lower than that for the Li/H or Fe/2H substitution.

Among other low-energy P/4H conformations, there is a symmetry-broken hh2 configuration with only two OH groups pointing inside the P tetrahedron, whereas the O1−H and O3−H groups point to the tet4 and oct2 voids, respectively. This configuration has slightly lower substitution energy of 0.51 eV per H atom. There are also w1 and w2 configurations, in which the OH groups change their arrangements in such a way so as to form one water molecule at the O1 site. However, their formation energy is higher by 0.04−0.07 eV per H atom compared to that of the hh2 configuration.

Finally, we considered substitution of the P vacancy with 5 H ($w1_5$), which maintains the charge balance of LFP and does not produce any small polaron. The configuration also contains one water molecule at the O1 site. The E_{sub} for this configuration is lower than that for 2hh by 0.07 eV/atom H.

The dependence of the substitution energy as a function of oxygen chemical potential for the studied stability range is shown in Figure 3. It is seen that the substitution of P with 4H is

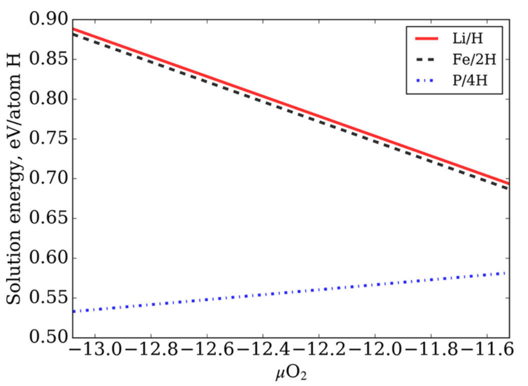

Figure 3. Energies of substitutions for Li/H, Fe/2H, and P/4H calculated with GGA+*U* as a function of O_2 chemical potential.

always easier than that for Li or Fe, especially for more reducing conditions. Also, the proportionality of E_{sub} with respect to the oxygen chemical potential has different signs for Li/H (Fe/2H) and P/4H. In particular, in a more oxidizing environment, the formation of Li/H (Fe/2H) defects could become favorable; however, this would be beyond the stability region of LFP.

The substitution energy of 0.53 eV can be compared with the P vacancy formation energy of 4.83 eV, from which it is seen that in the presence of water vapor, the formation of P vacancies stabilized by OH groups is more favorable.

3.6. Comparison of GGA and GGA+*U* Formation Energies. Table 3 compares GGA and GGA+*U* formation energies, calculated with respect to phases retrieved from the Li−Fe−P−O phase diagram constructed using the GGA+*U* functional. Since GGA+*U* results are in a better agreement with the experiment, the comparison of GGA and GGA+*U* allows for estimating the validity of the GGA approach for calculation of point defect formation energies. According to Table 3, the GGA functional fails to describe correctly formation energies of the Li and Fe vacancies. The GGA predicts negative energies, which corresponds to the instability of the LFP phase under the given conditions. Despite this, the comparison of defect geometries shows excellent similarity between the two approaches.

The substitution energies of the P/4H defects weakly depend on the used functional, while the relative energies are in a good agreement between GGA and GGA+*U*. For example, the hh2 structure is predicted to be lower than hh1 by 40 meV by both GGA and GGA+*U*; the geometries of defects are also almost identical. The local stabilization of the selected configurations with water molecules w1 and w2 was possible only using the GGA+*U* method, while GGA caused their decomposition into individual OH groups. The higher stability of metastable configurations in DFT+*U* is expected due to the stronger localization of the electron density. Overall, we conclude that the GGA functional is suitable for molecular dynamics study of the OH defects in the sense that deviations in relative energies of different configurations of the same defect between GGA and GGA+*U* are comparable with the accuracy of GGA+*U* itself.

4. MOLECULAR DYNAMICS STUDY OF OH DEFECTS

The static analysis of low-energy hydrogen defects in $LiFePO_4$ shows that the configurational space of such defects is rich enough for dynamic and entropic effects to be taken into consideration. We have conducted ab initio molecular dynamics (MD) simulations to study this system at the scale of tens of picoseconds, which turns out to be sufficient to observe transformations between most of the above-considered configurations at elevated temperatures. Thermogravimetric analysis showed that the water was not completely eliminated from the defective LFP samples up to 923 K;[18] therefore, we chose 900 K as the relevant temperature for our MD study. We start MD with relaxed geometries, and under these conditions, the considered 1 × 2 × 2 supercell comes to a local quasi-equilibrium already within 1 ps (see the typical dynamics of the free energy in Figure S12).

The first important observation inferred from MD trajectories is that hydrogens are always bonded to oxygen or iron atoms. In the particular case of oxygens, the standard deviation of the distance from a given hydrogen to the nearest oxygen is below 0.1 Å (see, e.g., Figure S8), whereas in transient configurations, the O−H−O separations are below or within the typical range of distances of hydrogen bonding (1.97 Å in water; see, e.g., Figure S10). Only one or two hydrogen atoms can be simultaneously bonded to a given oxygen atom, which is in agreement with our static calculations and the covalent nature of O−H bonds. Also, in accordance with the rules of hypervalent bonding, an attachment of the second hydrogen weakens the Fe−O bond; see Figures S18 and S25.

4.1. H in Ideal LFP and at Li and Fe Vacancies. With the abovementioned observations kept in mind, the analysis of the MD trajectories becomes straightforward. Starting with the case

https://doi.org/10.1021/acs.inorgchem.0c03241
Inorg. Chem. 2021, 60, 5497−5506

of a single hydrogen in the defect-free $LiFePO_4$, we see its diffusion through the lattice already at the timescale of tens of picoseconds, though a rigorous statistical analysis of the diffusion process requires more elaborated sampling, which is beyond the scope of this work. In the present work, we consider only one starting geometry per defect type: for the H interstitial, it is the lowest-energy configuration bonded to the Fe atom, H_i(t2) (hydrogen is near the Li-diffusion saddle point). With 10 × 10 ps MD sampling, we observe most of the transitions between the above discussed low-energy configurations. Two types of hydrogen dynamics are observed. The first is the motion inside the cage centered around the Li-diffusion saddle point. In this case, the hydrogen is almost always bonded to a single Fe atom (the one which is closest to the saddle point) with occasional bonding to other atoms, mostly other Fe atoms; see Figure S5. The second type is the diffusive motion along the *b* axis (the Li-diffusion channel). In this case, the hydrogen is alternatingly linked to the O1 and O2 oxygens with a simultaneous displacement of the adjacent Li atom; see Figure S6. The transition from Fe-bound dynamics to the oxygen-bound one occurs through O3−H configurations; see Figure S6. The reverse transition has not been observed because a longer simulation time or different initial configuration is required.

All other considered OH defects are based on lattice vacancies, and hydrogens are localized at the vacancies without escaping them on the considered timescale (10 runs, 10 ps each). In particular, for the H in Li vacancy, there are six centrally symmetric oxygen sites, which can be divided into two groups: triple of the sites O1, O2, and O3 and the symmetry-equivalent triple. It turns out that the two groups of sites are separated by a large potential energy barrier so that at the considered MD scale no transition is observed between the two potential energy basins, whereas sites O1 and O3 are well-populated when we start MD with the most favorable O2 site; see Figures S9 and S10.

In the case of two H atoms in the Fe vacancy, the configurational space is more complex. However, under the considered MD conditions no formation of water or hydrogen molecules is observed (Figure S11); therefore the dynamics of this system reduces to the motion of individual H atoms between six oxygen sites with the population of different configurations qualitatively corresponding to static calculations without entropy.

4.2. Four and Five H at P Vacancy.

In full agreement with static calculations, the observed dynamics of the P/4H defect involves only a change of orientations of the OH groups and formation of the H_2O molecule (bonded to Fe). The spatial distribution of each H in the case of P/4H defect is shown in Figure S20. Due to the steric constraints, at least one OH group is directed out of the P vacancy site but no more than two groups because of the energy penalty (Figure S19). As for the water molecule, it is temporarily formed at the O1 site for up to 1 ps (Figure 4), often ending up with H exchange (Figure 5). The main reason for the instability of the water molecule in $LiFePO_4$ is a crowded atomic environment. To support this thought, we considered a fully deintercalated material. Now, the structure and evolution of the P/4H defect are contrastingly different: the water molecule becomes stable at positions O1 and O2 and is also observed at position O3. This result is also consistent with our previous simulations of water molecules in nanocages of minerals.[46,47]

The static calculations using GGA confirm that the H_2O molecule in $FePO_4$ is more stable than separate OH groups by

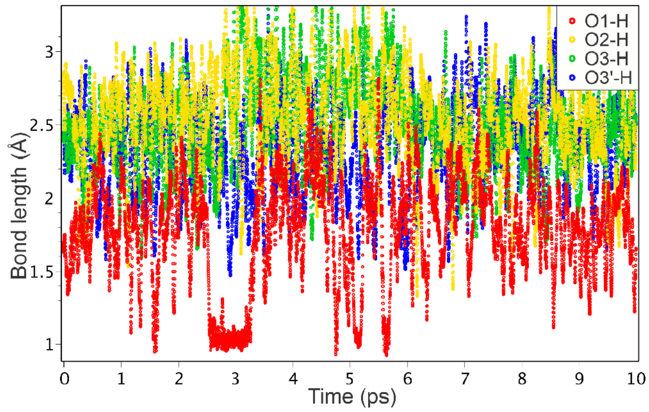

Figure 4. Dynamics of the O−H distance to the second-nearest hydrogen in the P/4H defect. Temporal formation of a water molecule is seen between 2.5 and 3.5 ps, where O1 attaches to the second hydrogen at a 1 Å distance.

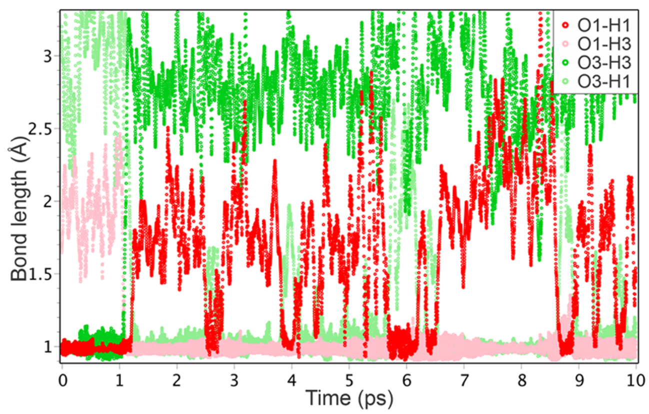

Figure 5. Dynamics of the O−H distances in the P/4H defect showing exchange of the two H atoms between O1 and O3 sites. In the legend, hydrogen atoms are labeled according to the oxygen atoms that they are initially attached to.

0.15 eV per H atom. However, in the case of GGA+*U*, the 4OH is still more stable than $2H_2O$ (by 0.1 eV per H atom). The latter may be explained by a larger penalty required to elongate the $Fe-OH_2$ bond and to form two undercoordinated O3 in the GGA+*U* case. Also, the local geometry of both defects is somewhat different between GGA and GGA+*U*, which shows that in the deintercalated case the Hubbard correction has a larger impact on the OH defects and may deserve a more detailed study. Additionally, we have checked the influence of the DFT+*U* method and the size of the unit cell rescaled to the simulation temperature (Supporting Information Section S12). The results presented in Table S7 show no significant difference between the protocols for the chosen sampling procedure (10 trajectories, 10 ps each). Indeed, thermal fluctuations at 900 K are large enough to wash out smaller effects such, as thermal expansion or lowered accuracy of the electronic structure calculation usually adopted for MD simulations.

The phosphorus vacancy with 5 H atoms at equilibrium already contains one water molecule attached to the Fe atom; therefore, the dynamics involves two types of processes: the motion of the extra hydrogen between oxygen sites and the temporal creation of two water molecules. The population statistics (Table S3) shows that water molecules predominantly occupy sites O1 and O2 with nearly equal probability. The

https://doi.org/10.1021/acs.inorgchem.0c03241
Inorg. Chem. 2021, 60, 5497−5506

distribution of Fe−O bond lengths (Table S3 and Figure S26) and the inspection of the MD trajectories reveal that the water molecule at the O1 site is only weakly bonded to the Fe atom and often detaches from it. It should also be noted that the P/5H defect has an asymmetric equilibrium configuration: the water molecule at the O1 site has one hydrogen located on the O1−O3 line, whereas the other hydrogen looks out of the P vacancy tetrahedron in the direction of the O3' site. The relaxed environment keeps this asymmetry at the considered MD timescale so that the population statistics is asymmetric (Table S3).

5. EXPERIMENTAL CONFIRMATION

To confirm the presence of OH defects experimentally, we have examined a phosphorus-deficient sample of $LiFePO_4$, synthesized under hydrothermal conditions with a very low concentration of the LFP solution (<0.01 mol/L).[18] The crystal framework of the sample was studied using a structural Rietveld refinement on the combined neutron (ND) and X-ray diffraction (XRD) data (Figure 6 and Tables S4 and S5). The sample was enriched with ^7Li and D isotopes to improve the quality of the ND data collection. The ND data were acquired both at room temperature and at 5 K to investigate in more detail a potential deuterium ordering in LFP when thermal motions were minimal.

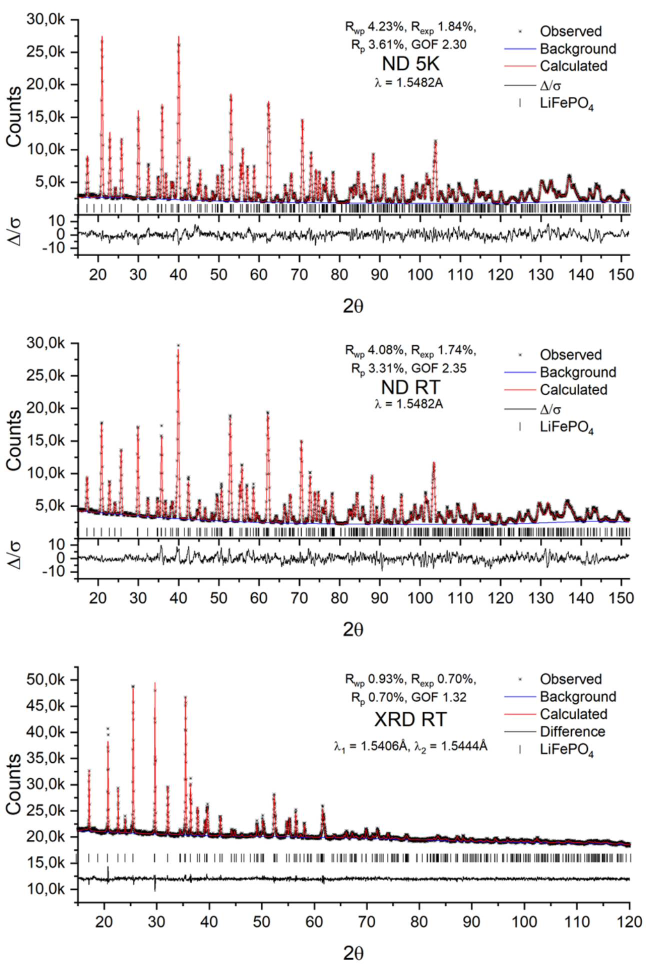

Figure 6. Observed, calculated, and difference plots for defect-rich $LiFePO_4$ via neutron (ND) and X-ray (XRD) diffraction experiments at 5 K and room temperature. Joint refinement indices are R_{wp} 1.72%, R_{exp} 0.92%, R_p 1.12%, and GOF 1.89.

The structure was refined in the $P2_1ma$ space group reported earlier for the P-deficient samples.[18] Two predominant iron sites were constrained to be equally occupied. The iron and lithium occupancies were allowed to refine freely, however, with coordinates being constrained to be the same. The phosphorus site occupancies were allowed to vary freely, though constrained to be equal. The sample revealed an antiferromagnetic ordering[48] at 5 K on the ND data, and it was refined with magnetic moments on the Fe sites constrained to a single absolute value. The structure at 5 K was refined in the magnetic space group $P2_1'ma'$ (26.69 in Shubnikov notation). The magnetic moment is aligned along the b-axis with 3.72(4) μ_B, which is close to our DFT+U calculated value of 3.77 μ_B (see Tables 1 and S6). The refined cell parameters at room temperature are a = 10.3453(2) Å, b = 6.0053(1) Å, c = 4.7022(1) Å, and V = 292.13(1) Å^3. The cell parameters at 5 K are a = 10.3175(1) Å, b = 5.9947(1) Å, c = 4.6899(1) Å, and V = 290.07(1) Å^3. The occupancy refinement demonstrated the presence of 6.6% of Fe at the Li site. The Li site also resulted in 7.9% of vacancies. The iron site occupancies converged with 100% of iron content leaving no room for other defects at this site. Phosphorus occupancies converged with 6% vacancies.

The presence of Li vacancies should result in phase separation, while P vacancies are highly unstable. Hence, both defects are expected to be stabilized by OD(OH) groups, as shown in the computational part of our study. According to the difference Fourier map constructed between the collected data and the refined model without hydrogen, the samples contained a residual scattering density, which can be attributed to deuterium. However, due to small occupancies and numerous splitting of D sites, the refinement of their coordinates was unsuccessful. Therefore, the positions of D atoms were taken from our DFT+U calculations for H. Interestingly, the computationally predicted positions coincided well with the majority of the most intensive residual density regions on the difference Fourier map (see Figure S28).

For Li/H and Fe/2H defects, the lowest-energy H positions were taken from the static calculations. For more disordered P/4H defects, we took 22 different snapshots from MD simulation and performed accurate DFT+U atomic relaxation at 0 K. The resulting locally stabilized H positions around each equivalent P site in the $Pnma$ symmetry are shown superimposed in Figure 7. First, we identified several H-rich regions around the P vacancy, which results in a variety of nonequivalent distributions of four hydrogens with close energies (the difference is within 0.01 eV/defect). Second, each H-rich region consists of numerous close-lying sites depending on the particular defect configuration, explaining the origin of instability during Rietveld refinement of their coordinates.

Therefore, up to 40 DFT+U predicted H sites were converted to align with $P2_1ma$ symmetry and introduced to the experimental unit cell refined on the ND data at 5 K. Their coordinates were set fixed and the occupancies were refined. All D sites refined with occupancies below three sigma levels were eliminated from the structure. The final structure resulted in nonzero occupancies for five nonequivalent D sites around the P site and three D sites around the Li site with low uncertainty. Since the Fe site converged with 100% iron content, the D sites around the Fe site were considered to be negligible and therefore eliminated from the refinement. The refined D sites should not be treated explicitly but rather as effective centers for numerous D(H) positions inside the H-rich regions. The final D sites are shown in Figure 7 and collected in Tables S4 and S5.

The resulting total composition of the sample converged with the content $Li_{0.86}D_{0.285}Fe_{1.065}P_{0.94}O_4$ with $D_{0.24}$ around the P site and $D_{0.045}$ around the Li site related to the Li/D ion exchange. Such a composition suggests 2.35% of Fe to be in the 3+ state to maintain the charge balance. This is in agreement with a previous study where according to Mössbauer spectroscopy the amount of Fe^{3+} in defective LFP is of the order of 4%.[18] Therefore, the predicted by DFT calculation stabilization of P vacancies in the LFP structure with OH defects is consistent with the refinement of the experimental diffraction data.

According to the refined composition, the amount of OD defects should be close to 3.2% by the mass. To investigate this, we performed a TGA study with analysis of the evolved gases by mass spectrometry.

https://doi.org/10.1021/acs.inorgchem.0c03241
Inorg. Chem. 2021, 60, 5497−5506

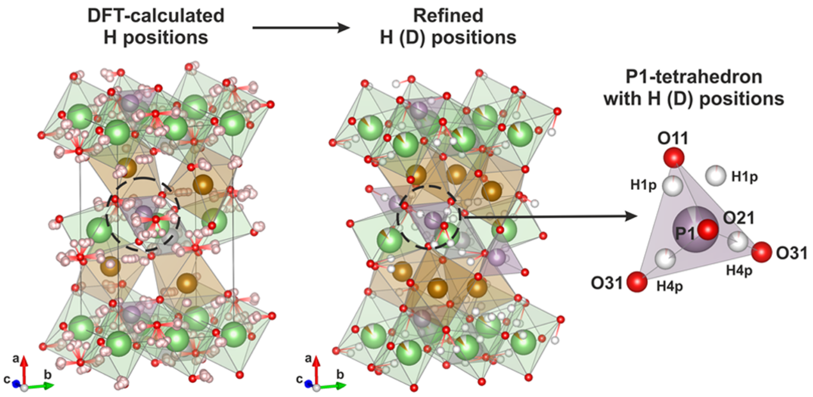

Figure 7. Left-hand side: Superimposed positions of H around each P in the unit cell with the *Pnma* symmetry for P/4H defects obtained by optimization at 0 K of 22 MD simulation snapshots. Right-hand side: the hydrogen sites left after joint refinement of their occupancies in the unit cell with $P2_1ma$ symmetry.

The detected mass loss corresponding to the OD emission amounted to ~2.9%, which is very close to the expected value (Figure S27).

6. DISCUSSION AND CONCLUSIONS

According to the thermodynamic model, based on the existing Li−Fe−P−O phase diagram in equilibrium with gaseous H_2O, the formation of individual H defects in $LiFePO_4$ is unfavorable (3.1 eV), while substitution of Li for H and Fe for 2H looks possible with substitution energy of 0.7−0.9 eV/atom H. The substitution of 4H and 5H for P is the most favorable process with substitution energy of 0.44−0.6 eV/atom H. We suggest that under experimental conditions of hydrothermal synthesis, the substitution energies can be lowered even further due to a number of factors. In our analysis, we neglect the vibrational entropy of hydrogen in solid phases, which should additionally stabilize solid phases compared to gas. Also, the Li−Fe−P−O_2 phase diagram in the presence of water can contain a number of unaccounted phases,[49] which can shift the calculated chemical potentials and the corresponding solution and substitution energies. In particular, we have considered the possibility of $LiFePO_4OH$ tavorite-phase formation for the considered conditions. It turns out that at most oxidizing oxygen potentials, the tavorite phase becomes slightly more stable than OH-defective LFP (by 0.1 eV/atom H); however, with the lowering of $\mu(O_2)$, the tavorite is destabilized and at most reducing conditions becomes less stable than OH-defective LFP by 0.3 eV/atom H. Indeed, the analysis of experimental XRD patterns shows no diffraction peaks related to the competing tavorite phase. Overall, our computational results reveal that the hydrogen incorporation into $LiFePO_4$ is a feasible process, and, among possible options, the substitution of H for P with the formation of hydrogarnet-like defects is the most favorable process.

Three types of interatomic interactions determine the structure and dynamics of hydroxyl defects in $LiFePO_4$. The strongest is the covalent bonding: hydrogens are always bonded to oxygens forming either an OH bond or two OH bonds in the geometry of the water molecule. The number of OH bonds depends on the number of bonds already attached to a given oxygen (not counting Li, which does not form strong covalent bonds in $LiFePO_4$). The orientation of OH bonds is determined by the electrostatic interaction subject to steric constraints. In a crowded atomic environment such as $LiFePO_4$, there is room only for single OH bonds, whereas in the presence of large voids such as in $FePO_4$, the water molecule is energetically more favorable (in GGA) than a pair of single OH bonds. In particular, the O1 and O2 oxygens in $LiFePO_4$ with a P vacancy have only a single bond with Fe; therefore, they readily accept two hydrogens forming a water molecule attached to Fe by a weak bond, elongated from 1.7 Å for a single oxygen atom to 2.0−2.3 Å for H_2O. The H_2O configuration is stable only if there are no steric constraints from the two Li atoms surrounding every oxygen atom in $LiFePO_4$. The O3 oxygen has two Fe−O bonds and thus its affinity to hydrogen is substantially lower than for the O1 and O2 oxygens. For $LiFePO_4$ with the P vacancy, the detailed energetical balance makes the “flagged pyramid” configuration the most stable one (the hydrogen attached to O1 looks out of the P vacancy tetrahedron, whereas all other hydrogens are directed toward O1). The “flag” is at O1 because, among all oxygens, it has the largest empty space (tet2) outside the P tetrahedron to host hydrogen with minimal steric constraints. When Li is removed, the configuration with two water molecules at the O1 and O2 sites becomes energetically more favorable. From a practical perspective, the obtained results show an efficient mechanism of water loss from hydrogenated $LiFePO_4$: at the surface, undercoordinated oxygens not bonded to phosphorus attract two hydrogens forming a water molecule, weakening the Fe−O bond and leading to the water molecule detachment. A rigorous confirmation of this mechanism requires MD simulations of the defective surface and accurate evaluation of the relative stability of OH and H_2O configurations, which is beyond the scope of the current study.

The accurate optimization of 22 snapshots taken from the MD simulation showed that even at 0 K, the P/4H defects have several nearly energetically degenerate configurations with particular H positions splitting into many close-lying sites easily affected by neighboring defects. This explains why hydroxyl defects are difficult to observe with diffraction-based methods. However, having employed the H coordinates predicted by DFT, we were able to refine the occupancy of the effective H positions with meaningful accuracy in the case of neutron diffraction data collected at low temperatures. Therefore, in combination with computational support, the diffraction-based methods can be successfully used for studying hydrogen defects in ionic crystals even at relatively small concentrations. Another prospective method that can potentially provide direct observation of hydroxyl defects inside the crystal lattice is atomic probe tomography, which is still under development for this class of materials.

https://doi.org/10.1021/acs.inorgchem.0c03241
Inorg. Chem. 2021, 60, 5497−5506

■ ASSOCIATED CONTENT

Supporting Information

The Supporting Information is available free of charge at https://pubs.acs.org/doi/10.1021/acs.inorgchem.0c03241.

Atomic coordinates for DFT+*U*-optimized structures (ZIP)

Additional figures and tables referenced in the text using "S" prefix, e.g., Figure S1 or Table S1 (PDF)

■ AUTHOR INFORMATION

Corresponding Author

Dmitry A. Aksyonov − *Skolkovo Institute of Science and Technology, 121205 Moscow, Russian Federation;* orcid.org/0000-0002-3692-4809; Email: d.aksenov@skoltech.ru

Authors

Irina Varlamova − *Skolkovo Institute of Science and Technology, 121205 Moscow, Russian Federation*

Ivan A. Trussov − *Skolkovo Institute of Science and Technology, 121205 Moscow, Russian Federation*

Aleksandra A. Savina − *Skolkovo Institute of Science and Technology, 121205 Moscow, Russian Federation*

Anatoliy Senyshyn − *Forschungsneutronenquelle Heinz Maier-Leibnitz (FRM II), Technische Universität München, 85747 Garching, Germany;* orcid.org/0000-0002-1473-8992

Keith J. Stevenson − *Skolkovo Institute of Science and Technology, 121205 Moscow, Russian Federation;* orcid.org/0000-0002-1082-2871

Artem M. Abakumov − *Skolkovo Institute of Science and Technology, 121205 Moscow, Russian Federation;* orcid.org/0000-0002-7135-4629

Andriy Zhugayevych − *Skolkovo Institute of Science and Technology, 121205 Moscow, Russian Federation;* orcid.org/0000-0003-4713-1289

Stanislav S. Fedotov − *Skolkovo Institute of Science and Technology, 121205 Moscow, Russian Federation;* orcid.org/0000-0003-4348-6517

Complete contact information is available at: https://pubs.acs.org/10.1021/acs.inorgchem.0c03241

Notes

The authors declare no competing financial interest.

■ ACKNOWLEDGMENTS

This work was supported by the Russian Foundation for Basic Research (Grant No. 18-29-12097). The authors thank Heinz Maier-Leibnitz Zentrum (MLZ) for granting time at SPODI (Proposal 16308).

■ REFERENCES

(1) Padhi, A.; Nanjundaswamy, K.; Goodenough, J. Phospho-olivines as Positive-Electrode Materials for Rechargeable Lithium Batteries. *J. Electrochem. Soc.* **1997**, *144*, 1188−1194.

(2) Myung, S. T.; Komaba, S.; Kurihara, K.; Kumagai, N. Preparation of LiFePO4 as lithium intercalation compound by emulsion drying method. *Electrochemistry* **2003**, *71*, 177−179.

(3) Islam, M. S.; Driscoll, D. J.; Fisher, C. A.; Slater, P. R. Atomic-scale investigation of defects, dopants, and lithium transport in the LiFePO4 olivine-type battery material. *Chem. Mater.* **2005**, *17*, 5085−5092.

(4) Yamada, A.; Koizumi, H.; Nishimura, S.-i.; Sonoyama, N.; Kanno, R.; Yonemura, M.; Nakamura, T.; Kobayashi, Y. O. Room-temperature miscibility gap in LixFePO4. *Nat. Mater.* **2006**, *5*, 357−360.

(5) Delmas, C.; Maccario, M.; Croguennec, L.; le Cras, F.; Weill, F. *Materials For Sustainable Energy: A Collection of Peer-Reviewed Research and Review Articles from Nature Publishing Group*; World Scientific, 2011; pp 180−186.

(6) Hong, L.; Li, L.; Chen-Wiegart, Y.-K.; Wang, J.; Xiang, K.; Gan, L.; Li, W.; Meng, F.; Wang, F.; Wang, J. Two-dimensional lithium diffusion behavior and probable hybrid phase transformation kinetics in olivine lithium iron phosphate. *Nat. Commun.* **2017**, *8*, No. 1194.

(7) Hong, L.; Yang, K.; Tang, M. A mechanism of defect-enhanced phase transformation kinetics in lithium iron phosphate olivine. *npj Comput. Mater.* **2019**, *5*, No. 118.

(8) Maier, J.; Amin, R. Defect chemistry of LiFePO4. *J. Electrochem. Soc.* **2008**, *155*, No. A339.

(9) Song, M.-S.; Kang, Y.-M.; Kim, Y.-I.; Park, K.-S.; Kwon, H.-S. Nature of Insulating-Phase Transition and Degradation of Structure and Electrochemical Reactivity in an Olivine-Structured Material, LiFePO4. *Inorg. Chem.* **2009**, *48*, 8271−8275.

(10) Iturrondobeitia, A.; Goñi, A.; Gil de Muro, I.; Lezama, L.; Kim, C.; Doeff, M.; Cabana, J.; Rojo, T. High-Voltage Cathode Materials for Lithium-Ion Batteries: Freeze-Dried LiMn0.8Fe0.1M0.1PO4/C (M = Fe, Co, Ni, Cu) Nanocomposites. *Inorg. Chem.* **2015**, *54*, 2671−2678.

(11) Drozhzhin, O. A.; Sumanov, V. D.; Karakulina, O. M.; Abakumov, A. M.; Hadermann, J.; Baranov, A. N.; Stevenson, K. J.; Antipov, E. V. Switching between solid solution and two-phase regimes in the Li1-xFe1-yMnyPO4 cathode materials during lithium (de)-insertion: combined PITT, in situ XRPD and electron diffraction tomography study. *Electrochim. Acta* **2016**, *191*, 149−157.

(12) Love, C. T.; Korovina, A.; Patridge, C. J.; Swider-Lyons, K. E.; Twigg, M. E.; Ramaker, D. E. Review of LiFePO4 phase transition mechanisms and new observations from x-ray absorption spectroscopy. *J. Electrochem. Soc.* **2013**, *160*, No. A3153.

(13) Drozhzhin, O. A.; Sobolev, A. V.; Sumanov, V. D.; Glazkova, I. S.; Aksyonov, D. A.; Grebenshchikova, A. D.; Tyablikov, O. A.; Alekseeva, A. M.; Mikheev, I. V.; Dovgaliuk, I. Exploring the Origin of the Superior Electrochemical Performance of Hydrothermally Prepared Li-Rich Lithium Iron Phosphate Li1 + δFe1- δPO4. *J. Phys. Chem. C* **2020**, *124*, 126−134.

(14) Malik, R.; Zhou, F.; Ceder, G. Kinetics of non-equilibrium lithium incorporation in LiFePO 4. *Nat. Mater.* **2011**, *10*, 587−590.

(15) Axmann, P.; Stinner, C.; Wohlfahrt-Mehrens, M.; Mauger, A.; Gendron, F.; Julien, C. M. Nonstoichiometric LiFePO4: defects and related properties. *Chem. Mater.* **2009**, *21*, 1636−1644.

(16) Hoang, K.; Johannes, M. Tailoring native defects in LiFePO4: insights from first-principles calculations. *Chem. Mater.* **2011**, *23*, 3003−3013.

(17) Amisse, R.; Sougrati, M. T.; Stievano, L.; Davoisne, C.; Dražič, G.; Budič, B.; Dominko, R.; Masquelier, C. Singular Structural and Electrochemical Properties in Highly Defective LiFePO4 Powders. *Chem. Mater.* **2015**, *27*, 4261−4273.

(18) Sumanov, V. D.; Aksyonov, D. A.; Drozhzhin, O. A.; Presniakov, I.; Sobolev, A. V.; Glazkova, I.; Tsirlin, A. A.; Rupasov, D.; Senyshyn, A.; Kolesnik, I. V. "Hydrotriphylites" Li1-x Fe1+ x (PO4) 1-y (OH) 4 y as Cathode Materials for Li-ion Batteries. *Chem. Mater.* **2019**, *31*, 5035−5046.

(19) Khisina, N. R.; Lorents, K. A. Types of OH-bearing point defects in olivine and their transformation under changing petrological conditions. *Geochem. Int.* **2015**, *53*, 501−509.

(20) Beran, A.; Putnis, A. A model of the OH positions in olivine, derived from infrared-spectroscopic investigations. *Phys. Chem. Miner.* **1983**, *9*, 57−60.

(21) Hobbs, B. E. Point defect chemistry of minerals under a hydrothermal environment. *J. Geophys. Res.: Solid Earth* **1984**, *89*, 4026−4038.

(22) Brodholt, J. P.; Refson, K. An ab initio study of hydrogen in forsterite and a possible mechanism for hydrolytic weakening. *J. Geophys. Res.: Solid Earth* **2000**, *105*, 18977−18982.

(23) de Leeuw, N. H. Density functional theory calculations of hydrogen-containing defects in forsterite, periclase, and α-quartz. *J. Phys. Chem. B* **2001**, *105*, 9747−9754.

https://doi.org/10.1021/acs.inorgchem.0c03241
Inorg. Chem. 2021, 60, 5497−5506

(24) Dudnikova, V. B.; Urusov, V. S. Simulation of forsterite protonation by the interatomic potential method. *Geochem. Int.* **2014**, *52*, 261−270.
(25) Qin, T.; Wentzcovitch, R. M.; Umemoto, K.; Hirschmann, M. M.; Kohlstedt, D. L. Ab initio study of water speciation in forsterite: Importance of the entropic effect. *Am. Mineral.* **2018**, *103*, 692−699.
(26) Jain, A.; Shin, Y.; Persson, K. A. Computational predictions of energy materials using density functional theory. *Nat. Rev. Mater.* **2016**, *1*, No. 15004.
(27) Kresse, G.; Furthmüller, J. Efficiency of ab-initio total energy calculations for metals and semiconductors using a plane-wave basis set. *Comput. Mater. Sci.* **1996**, *6*, 15−50.
(28) Aksyonov, D. A.; Fedotov, S. S.; Stevenson, K. J.; Zhugayevych, A. Understanding migration barriers for monovalent ion insertion in transition metal oxide and phosphate based cathode materials: A DFT study. *Comput. Mater. Sci.* **2018**, *154*, 449−458.
(29) Perdew, J. P.; Burke, K.; Wang, Y. Generalized gradient approximation for the exchange−correlation hole of a many-electron system. *Phys. Rev. B* **1996**, *54*, 16533−16539.
(30) Dudarev, S. L.; Botton, G. A.; Savrasov, S. Y.; Humphreys, C. J.; Sutton, A. P. Electron-energy-loss spectra and the structural stability of nickel oxide: An LSDA+U study. *Phys. Rev. B* **1998**, *57*, 1505−1509.
(31) Jain, A.; Hautier, G.; Ong, S. P.; Moore, C. J.; Fischer, C. C.; Persson, K. A.; Ceder, G. Formation enthalpies by mixing GGA and GGA+ U calculations. *Phys. Rev. B* **2011**, *84*, No. 45115.
(32) Ong, S. P.; Wang, L.; Kang, B.; Ceder, G. Li- Fe- P- O2 phase diagram from first principles calculations. *Chem. Mater.* **2008**, *20*, 1798−1807.
(33) Hoelzel, M.; Senyshyn, A.; Dolotko, O. SPODI: High resolution powder diffractometer. *J. Large-Scale Res. Facil.* **2015**, *1*, No. 5.
(34) Coelho, A. TOPAS and TOPAS-Academic: an optimization program integrating computer algebra and crystallographic objects written in C++. *J. Appl. Crystallogr.* **2018**, *51*, 210−218.
(35) Zhou, F.; Cococcioni, M.; Marianetti, C. A.; Morgan, D.; Ceder, G. First-principles prediction of redox potentials in transition-metal compounds with LDA + U. *Phys. Rev. B* **2004**, *70*, No. 235121.
(36) Asari, Y.; Suwa, Y.; Hamada, T. Formation and diffusion of vacancy-polaron complex in olivine-type LiMnPO4 and LiFePO4. *Phys. Rev. B* **2011**, *84*, No. 134113.
(37) Zhou, F.; Kang, K.; Maxisch, T.; Ceder, G.; Morgan, D. The electronic structure and band gap of LiFePO4 and LiMnPO4. *Solid State Commun.* **2004**, *132*, 181−186.
(38) Bhowmik, A.; Sarkar, T.; Kumar Varanasi, A.; Waghmare, U. V.; Dixit Bharadwaj, M. Origins of electrochemical performance of olivine phosphate as cathodes in Li-ion batteries: Charge transfer, spin-state, and structural distortion. *J. Renewable Sustainable Energy* **2013**, *5*, No. 053130.
(39) Xiong, Z.-C.; Xie, Y.; Yi, T.-F.; Yu, H.-t.; Zhu, Y.-R.; Zeng, Y.-Y. Effect of lithium extraction on the stabilities, electrochemical properties, and bonding characteristics of LiFePO4 cathode materials: A first-principles investigation. *Ceram. Int.* **2014**, *40*, 2655−2661.
(40) Jena, A.; Nanda, B. R. K. Unconventional magnetism and band gap formation in LiFePO 4: Consequence of polyanion induced non-planarity. *Sci. Rep.* **2016**, *6*, No. 19573.
(41) Castro, L.; Dedryvere, R.; el Khalifi, M.; Lippens, P.-E.; Bréger, J.; Tessier, C.; Gonbeau, D. The spin-polarized electronic structure of LiFePO4 and FePO4 evidenced by in-lab XPS. *J. Phys. Chem. C* **2010**, *114*, 17995−18000.
(42) Hayward, M. A.; Cussen, E. J.; Claridge, J. B.; Bieringer, M.; Rosseinsky, M. J.; Kiely, C. J.; Blundell, S. J.; Marshall, I. M.; Pratt, F. L. The hydride anion in an extended transition metal oxide array: LaSrCoO3H0.7. *Science* **2002**, *295*, 1882−1884.
(43) Kobayashi, Y.; et al. An oxyhydride of BaTiO3 exhibiting hydride exchange and electronic conductivity. *Nat. Mater.* **2012**, *11*, 507−511.
(44) Maxisch, T.; Zhou, F.; Ceder, G. Ab initio study of the migration of small polarons in olivine Lix FePO4 and their association with lithium ions and vacancies. *Phys. Rev. B* **2006**, *73*, 1−6.
(45) Zaghib, K.; Mauger, A.; Goodenough, J. B.; Gendron, F.; Julien, C. M. Electronic, Optical, and Magnetic Properties of LiFePO4: Small Magnetic Polaron Effects. *Chem. Mater.* **2007**, *19*, 3740−3747.
(46) Belyanchikov, M. A.; et al. Dielectric ordering of water molecules arranged in a dipolar lattice. *Nat. Commun.* **2020**, *11*, No. 3927.
(47) Belyanchikov, M. A.; Zhukova, E. S.; Tretiak, S.; Zhugayevych, A.; Dressel, M.; Uhlig, F.; Smiatek, J.; Fyta, M.; Thomas, V. G.; Gorshunov, B. P. Vibrational states of nano-confined water molecules in beryl investigated by first-principles calculations and optical experiments. *Phys. Chem. Chem. Phys.* **2017**, *19*, 30740−30748.
(48) Dai, D.; Whangbo, M.-H.; Koo, H.-J.; Rocquefelte, X.; Jobic, S.; Villesuzanne, A. Analysis of the Spin Exchange Interactions and the Ordered Magnetic Structures of Lithium Transition Metal Phosphates LiMPO4 (M = Mn, Fe, Co, Ni) with the Olivine Structure. *Inorg. Chem.* **2005**, *44*, 2407−2413.
(49) Marx, N.; Bourgeois, L.; Carlier, D.; Wattiaux, A.; Suard, E.; Le Cras, F.; Croguennec, L. Iron(III) Phosphates Obtained by Thermal Treatment of the Tavorite-Type FePO4·H2O Material: Structures and Electrochemical Properties in Lithium Batteries. *Inorg. Chem.* **2012**, *51*, 3146−3155.

https://doi.org/10.1021/acs.inorgchem.0c03241
Inorg. Chem. 2021, 60, 5497−5506